THE JOURNAL OF PHYSICAL CHEMISTRY A

pubs.acs.org/JPCA Article

CLS Next Gen: Accurate Frequency−Frequency Correlation Functions from Center Line Slope Analysis of 2D Correlation Spectra Using Artificial Neural Networks

David J. Hoffman and Michael D. Fayer*

Cite This: J. Phys. Chem. A 2020, 124, 5979−5992 Read Online

ACCESS | Metrics & More | Article Recommendations | Supporting Information

ABSTRACT: The center line slope (CLS) observable has become a popular method for characterizing spectral diffusion dynamics in two-dimensional (2D) correlation spectroscopy because of its ease of implementation, robustness, and clear theoretical relationship to the frequency−frequency correlation function (FFCF). The FFCF relates the frequency fluctuations of an ensemble of chromophores to coupled bath modes of the chemical system and is used for comparison to molecular dynamics simulations and for calculating 2D spectra. While in the appropriate limits, the CLS can be shown to be the normalized FFCF, from which the full FFCF can be obtained, in practice the assumptions that relate the CLS to the normalized FFCF are frequently violated. These violations are due to the presence of homogeneous broadening and motional narrowing. The generalized problem of relating the CLS to the FFCF is reanalyzed by introducing a new set of dimensionless parameters for both the CLS and FFCF. A large data set was generated of CLS parameters derived from numerically modeled 2D line shapes with known FFCF parameters. This data set was used to train feedforward artificial neural networks that act as functions, which take the CLS parameters as inputs and return FFCF parameters. These neural networks were deployed in an algorithm that is able to quickly and accurately determine FFCF parameters from experimental CLS parameters and the fwhm of the absorption line shape. The method and necessary inputs to accurately obtain the FFCF from the CLS are presented.

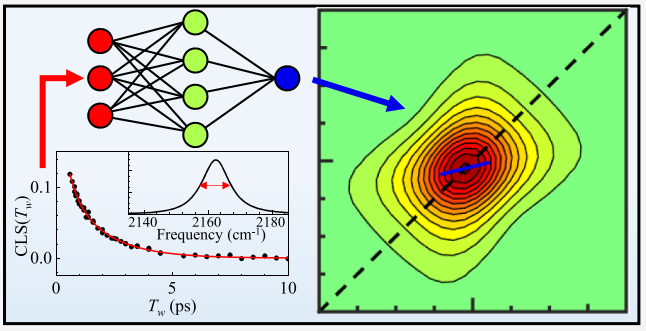

1. INTRODUCTION

Two-dimensional correlation spectroscopy (2D CS) has become a powerful tool for studying the dynamics of a wide range of chemical systems. While developed first in 2D nuclear magnetic resonance,[1] ultrafast laser equipment has enabled 2D CS to be performed in the infrared[2,3] (2D IR) and more recently for electronic spectroscopy at ultraviolet/visible frequencies (2D ES).[4,5] 2D IR spectroscopy has been used to examine the dynamics of liquids[2,6−8] and solute−solvent interactions,[9−12] protein dynamics,[13,14] and even the dynamics of crystalline solids[15,16] and interfaces.[17,18] The development of 2D ES has permitted the study of photoactive systems including dye molecules,[19] photovoltaics,[20,21] quantum dots and wells,[22,23] and photosynthetic pathways.[24−27] A large family of related techniques are also being developed, including 2D electronic-vibrational[28] and vibrational-electronic,[29] heterodyne-detected 2D vibrational sum frequency generation,[30,31] and 2D terahertz,[32] which all arise from the same theoretical framework.[33]

A 2D CS spectrum is a correlation plot between the frequencies of an ensemble of chromophores at an initial time and the frequencies of the chromophores after a "waiting time" T_w.[2,3] There is a high density of information in a 2D spectra, such as the appearance of cross peaks from coherence transfer[34,35] or chemical exchange[9,10,36] and decay in the amplitudes of peaks due to population relaxation and orientational relaxation.[37] Of particular interest in 2D IR,[2] and increasingly in 2D ES,[24] is the time evolution of the 2D line shape. If the spectrum is inhomogeneously broadened, the distribution of frequencies in the line shape typically corresponds to the distribution of chemical environments of the chromophore. This correlation causes the 2D line shape at short times to appear elongated along the diagonal. The time evolution of the chemical system can then cause the chemical environments of the chromophores to change, which decorrelates the frequencies of the chromophores in a process called "spectral diffusion". Spectral diffusion causes the frequency of the chromophores to randomize within the inhomogeneous spectrum, which results in the 2D spectra becoming rounder as the waiting time T_w increases.

Received: May 13, 2020
Revised: June 17, 2020
Published: June 18, 2020

Downloaded via STANFORD UNIV on August 8, 2020 at 22:11:54 (UTC).
See https://pubs.acs.org/sharingguidelines for options on how to legitimately share published articles.

ACS Publications © 2020 American Chemical Society

https://dx.doi.org/10.1021/acs.jpca.0c04313
J. Phys. Chem. A 2020, 124, 5979−5992

The process of spectral diffusion is quantitatively described by the frequency−frequency correlation function (FFCF).[33] The FFCF is the probability that a chromophore with a given frequency at time zero will have the same frequency at a time T_w later, averaged over the entire inhomogeneous spectra. In the appropriate limits, the FFCF also provides the connection between the given mode and the dynamics of the bath modes that drive spectral diffusion. The FFCF is then the critical connection between the experimentally observed 2D line shapes and the underlying dynamics of the chemical system. This connection also provides a fundamental relationship between 2D CS studies and molecular dynamics simulations.[6,38−42] Knowledge of the FFCF is also necessary to accurately employ analytic theories that describe the FFCF, such as in reorientation-induced spectral diffusion (RISD).[43]

Despite the importance of the FFCF, it is difficult to extract because of the nature of 2D line shape analyses. The center line slope (CLS) method[44,45] has become prominent in recent years because of its ease of implementation, robustness to common artifacts and line shape distortions, and clear theoretical underpinning to the FFCF. The CLS has been extended to account for a variety of other effects, including non-Gaussian dynamics,[46] two component line shapes,[47] and some of the phenomenology of 2D ES spectroscopy.[48,49] The CLS technique works by taking slices of a 2D spectrum along one of the frequency axes at a fixed time T_w around the center of the spectrum. The maximum of each slice is then connected into the center line. In the limit where the 2D spectrum is purely Gaussian, the slope of the center line with respect to the frequency axis will be proportional to the normalized FFCF at that time T_w. By repeating the procedure at each measured T_w, the time dependent normalized FFCF can be extracted for the chemical system.

However, the direct analytical relationship between the CLS analysis and the FFCF is only valid if the 2D line shape is purely inhomogeneously broadened.[44,45] All experimental 2D spectra also have homogenous broadening from a combination of lifetime broadening, rotational broadening, and motional narrowing. Further, some dynamic processes can be partially motionally narrowed, effectively contributing both an inhomogeneous and homogeneous component to the total line shape. Both homogeneous broadening and partial motional narrowing make the 2D line shape equations analytically intractable and cause the CLS to deviate from the normalized FFCF. Partial motional narrowing can be particularly deceiving. Although the FFCF time constants are correct, partial motional narrowing changes the relative amplitudes of various inhomogeneous components and can give a false impression of the relative significance of different dynamical time scales. This effect causes the CLS to no longer be proportional to the FFCF, and generally causes the algorithmic approach for recovering the FFCF in the original CLS paper to be inaccurate.[44]

In this work a new procedure for extracting the FFCF from CLS analysis is presented. The new algorithm is based on the empirical observation that the time constants measured by the CLS match those in the FFCF, while the amplitudes of the CLS components will scale based on the relative amplitudes of the FFCF components and the degree of motional narrowing of the FFCF components. A new set of dimensionless parameters are motivated for both the FFCF and CLS that reflect the relative amplitudes and relative degree of motional narrowing of different line shape components. These new parameters associate a set of FFCFs with a single rescaled CLS decay. The rescaled FFCFs are then distinguishable by the full width at half-maximum (fwhm) of the associated absorption spectra. The rescaling greatly reduces the overall FFCF parameter space. The new parameters also help in determining if an experimentally measured line shape component is partially motionally narrowed and immediately enables determination of the FFCF from the CLS in the absence of partial motional narrowing.

In the presence of partial motional narrowing, the new FFCF and CLS parameters were found to have a highly nonlinear relationship with each other. To fully characterize the relationship between the FFCF and CLS, the CLS was extracted from 250,000 sets of numerically modeled 2D line shapes with a wide range of FFCF parameters. The results of these calculations were used to train artificial neural networks (ANNs) that serve as functions that take the new CLS parameters as inputs and returns the corresponding FFCF parameters. By combining the new FFCF parameters determined by the ANNs with experimentally determined time constants and the fwhm of the linear spectrum, the experimental FFCF can be quickly and accurately calculated. The complete algorithm will also be available as a standalone application, (CLS ANN FFCF Extractor or CAFE) for free download at the URL provided in the ref 50. This algorithm completes the relationship between the CLS and FFCF for Gaussian relaxation dynamics, which is the basis for the widely used diagrammatic perturbation theory of nonlinear spectroscopy,[33] employed in the original development of the CLS method.[44]

2. THEORETICAL BACKGROUND OF THE CLS METHOD

2.1. Response Functions and the FFCF. The linear absorption line shape can be determined by taking the real part of the Fourier transform of the first order response function $R^1(t)$. Following the Kubo model for line shapes in the Condon approximation, the linear first order response function is given by[3,33]

$$R^1(t) \propto \left\langle \exp\left(-i\int_0^t \mathrm{d}\tau\omega(\tau)\right)\right\rangle \tag{1}$$

where $\omega(\tau)$ is a fluctuating transition frequency. Analogously, the 2D spectra for a given transition can be obtained from the nonlinear third order response functions[3,33]

$$R_{\mathrm{N,R}}{}^3(t_1, T_w, t_3) \propto \left\langle \exp\left(\pm i\int_0^{t_1} \mathrm{d}\tau\omega(\tau) - i\int_{T_w}^{T_w+t_3} \mathrm{d}\tau'\omega(\tau')\right)\right\rangle \tag{2}$$

where R_N and R_R are the nonrephasing (negative first term) and rephasing (positive first term), respectively. To get the corresponding absorptive 2D spectrum, both R_N and R_R are Fourier transformed along the coherence times, t_1 and t_3. The two double Fourier transforms are then summed together to get the final absorptive 2D spectrum.

The above expressions are evaluated by using the cumulant expansion of the ensemble average truncated at second order. This allows the linear and nonlinear response functions to be rewritten in terms of a single line shape function, $g(t)$[3,33]

$$g(t) = \int_0^t \mathrm{d}\tau_2 \int_0^{\tau_2} \mathrm{d}\tau_1 \langle \delta\omega(\tau_1)\delta\omega(0)\rangle \tag{3}$$

where $\langle \delta\omega(\tau_1)\delta\omega(0)\rangle$is the FFCF for the given transition frequency. This result uses the generally accurate assumption that the FFCF can be described using Gaussian processes of a

https://dx.doi.org/10.1021/acs.jpca.0c04313
J. Phys. Chem. A 2020, 124, 5979−5992

classical stochastic variable $\delta\omega$, such that the entire behavior can be entirely characterized by a two-point correlation function. In Section 5 it will be demonstrated that this assumption still works to describe the diffusive part of the FFCF for quantum Gaussian processes. The first order response function is then given by[3,33]

$$R^1(t) \propto \exp(-i\langle\omega\rangle)\exp(-g(t)) \tag{4}$$

The third order response functions have analogous, lengthy expressions that depend on evaluating the line shape function at the three time intervals t_1, T_w, and t_3 as well as at sums of these intervals. The complete expressions can be found elsewhere.[3,33,44]

The FFCF itself is typically described as a sum of exponential decays

$$C(t) = \langle\delta\omega(t)\delta\omega(0)\rangle = \frac{\delta(t)}{T_2} + \sum_i \Delta_i{}^2\exp(-t/\tau_i) \tag{5}$$

where τ_i corresponds to the timescale of the decay for the ith component, Δ_i corresponds to the standard deviation of frequencies sampled for the ith component, $\delta(t)$ is the Dirac delta function, and T_2 is the homogeneous dephasing time. T_2 can also be described using the homogeneous line width, $\Gamma = (\pi T_2)^{-1}$, which allows a direct comparison to the inhomogeneous Δ components.

2.2. Short Time Approximation and the CLS. For the Fourier transforms containing the line shape function to be analytically tractable, two approximations are made.[44] First, the homogeneous line width is set equal to zero, that is, $\Gamma = (\pi T_2)^{-1} = 0$. Next, the line shape functions are expanded to second order in the coherence times, for example,

$$g(t) = \int_0^t d\tau_2 \int_0^{\tau_2} d\tau_1 \Delta^2 \exp(-\tau_1/\tau)$$

$$g(t) = \Delta^2\tau t + \Delta^2\tau^2(\exp(-t/\tau) - 1) \approx \Delta^2 t^2/2 \tag{6}$$

The short time approximation implicitly assumes that spectral diffusion is slow, so that the quantity $\Delta\tau \gg 1$. This approximation inherently neglects the effects of motional narrowing from fast dynamics, which will be examined in a later section. From eq 6 and the definitions of the cumulant-expanded third order response functions,[3,33,44] it is straightforward to show that the absorptive line shape goes as[44]

$$R^g(\omega_1, T_w, \omega_3) = \frac{2\pi}{\sqrt{C^2(0) - C^2(T_w)}} \exp\left(-\frac{C(0)(\omega_1{}^2 + \omega_3{}^2) - 2C(T_w)\omega_1\omega_3}{2(C^2(0) - C^2(T_w))}\right) \tag{7}$$

From which the principle CLS results can be readily derived[44,45]

$$\left.\frac{\partial R^g(\omega_1, T_w, \omega_3)}{\partial\omega_1}\right|_{\omega_1=\omega_1^{max}} = 0 \rightarrow \text{CLS } \omega_3(T_w) = \frac{d\omega_1^{max}(\omega_3)}{d\omega_3} = \frac{C(T_w)}{C(0)}$$

$$\left.\frac{\partial R^g(\omega_1, T_w, \omega_3)}{\partial\omega_3}\right|_{\omega_3=\omega_3^{max}} = 0 \rightarrow \text{CLS } \omega_1(T_w) = \frac{d\omega_3^{max}(\omega_1)}{d\omega_1} = \frac{C(T_w)}{C(0)} \tag{8}$$

The first equation shows that by first finding the position of the maximum along each frequency ω_1 as a function of ω_3, and then finding the slope of the line made by the maxima of ω_1 with respect to ω_3 (CLS ω_3 or ω_m), one rigorously obtains the normalized FFCF. The second equation shows that the same result is true when the frequency axes are switched (CLS ω_1 or ω_τ). Correlated ($C(T_w)/C(0) = 0.8$) and decorrelated ($C(T_w)/C(0) = 0$) calculated 2D spectra are shown in Figure 1 with the CLS ω_3 in blue and the CLS ω_1 in gray. The symmetry of the equations arise from the symmetry of the 2D spectra with regards to the diagonal $\omega_1 = \omega_3$ (dashed lines in Figure 1), which is in turn due to the symmetry of t_1 and t_3 in the third order response functions. The fact that the two measurements generally yield the same result can also be used as a test that the experimental data is free from systematic errors that would preferentially distort one frequency axis.

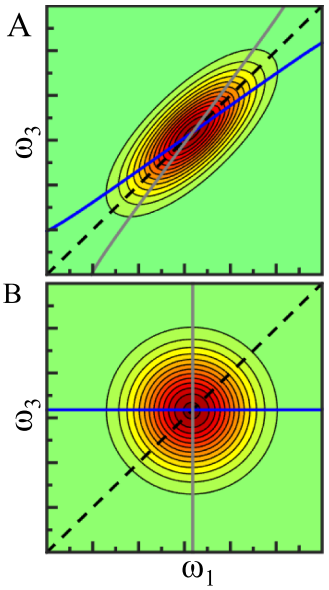

Figure 1. (A) Example 2D spectrum in the short-time approximation limit described by eq 7. $C(T_w)/C(0) = 0.8$, indicating high correlation in the FFCF. The dashed line is the diagonal, $\omega_1 = \omega_3$, which illustrates the symmetry of the 2D line shape. The blue line is the CLS ω_3 and the gray line is CLS ω_1, as defined by eq 8. Both lines have slope 0.8 with respect to the appropriate axis. (B) 2D spectrum as given by eq 7 where $C(T_w)/C(0) = 0$, indicating no correlation in the FFCF.

3. CHARACTERIZING THE CLS BEYOND THE ANALYTICAL LIMIT

3.1. Procedure for Numerically Calculating 2D Spectra. To go beyond the analytically solvable limits of the CLS described in Section 2, it is necessary to numerically calculate the line shapes for arbitrary FFCFs. For an FFCF as determined by the Δ_i, τ_i, and T_2 in eq 5, the third order response functions were calculated at select T_w's. To avoid accidental apodization, the range for the coherence times was extended until the rephasing function for $T_w = 0$ was below 0.005, that is, $R_R{}^3(t_{max}, T_w = 0, t_{max}) \leq 0.005$. The time ranges t_1 and t_3 were then discretized into 100 equally spaced intervals. The time domain response functions were then numerically Fourier transformed along both the t_1 and t_3 axes to obtain the corresponding 2D spectra for each of the T_w's. The CLS as a function of T_w was then calculated from the 2D spectra along ω_3. The CLS decay was parameterized in an analogous manner to the FFCF

$$\text{CLS}(T_w) = \sum_i A_i \exp(-T_w/\tau_i) \tag{9}$$

https://dx.doi.org/10.1021/acs.jpca.0c04313
J. Phys. Chem. A 2020, 124, 5979−5992

where A_i is the normalized amplitude of the spectral diffusion process as measured by the CLS observable, T_w is the waiting time of the 2D experiment, and τ_i corresponds to the timescale of a spectral diffusion process, which we will show is identically the τ_i in the FFCF (eq 5).

3.2. Homogeneous Component. As was described in the original CLS paper,[44] the introduction of a homogeneous component to the FFCF will cause the CLS to start below a perfect correlation of 1 at $T_w = 0$. This result could be predicted based on the definition of the FFCF (eq 5) and the CLS (eq 9). However, the resulting CLS can also be seen to not correspond to the FFCF normalized to its value at $T_w = 0$.

In the absence of inhomogeneous broadening, the purely homogeneous 2D line shape will be a T_w-independent 2D Lorentzian[3,48]

$$R^{L}(\omega_1, T_w, \omega_3) = \frac{1}{\pi}\frac{(1/T_2)^2}{((1/T_2)^2 + \omega_1^2)((1/T_2)^2 + \omega_3^2)} \tag{10}$$

The complete 2D line shape in the presence of both purely homogeneous broadening and a slow inhomogeneous component is then the 2D convolution of the 2D Lorentzian in eq 10 and the correlated 2D Gaussian in eq 7. Unfortunately, the resulting 2D correlated Voigt line shape is as analytically intractable as its one-dimensional (1D) counterpart.

Calculating the derivatives to find the CLS values as was done in eq 8 for the Gaussian line shape shows that the 2D Lorentzian has a CLS of zero. This suggests that a reasonable approximation could be made for the 2D convolution by approximating the Lorentzian contribution as an uncorrelated 2D Gaussian:

$$R^{L}(\omega_1, T_w, \omega_3) \approx \frac{2\pi}{(1/T_2)}\exp\left(-\frac{(\omega_1^2 + \omega_3^2)}{2((1/T_2)^2)}\right) \tag{11}$$

which is equivalent to replacing the homogeneous part of the time domain line shape function, t/T_2, with $t^2/(2T_2^2)$. The convolution of eq 11 with eq 7 can then be solved analytically. Sample line shapes comparing calculated 2D Voigt with the 2D Gaussian approximations with their CLS curves can be seen in Figure 2A. It can be seen the Gaussian approximation captures the behavior of the CLS near the peak center, the region used for analysis of experimental data, although it misses nonlinearities in the CLS introduced in the wings by the Lorentzian component. Analytically calculating the CLS for the approximated line shape gives the following prediction for the CLS

$$\mathrm{CLS}(T_w) \approx \frac{\sum_i \Delta_i^2 \exp(-T_w/\tau_i)}{(1/T_2)^2 + \sum_i \Delta_i^2} \tag{12}$$

This prediction is plotted against the CLS calculated for 2D line shapes with time-independent inhomogeneous broadening for a range of homogeneous and inhomogeneous components in Figure 2B (black points). For highly inhomogeneous line shapes (CLS > ~0.5) the approximation is excellent, and the approximation remains good even when the FFCF has a large homogeneous contribution. Significantly, a comparison of the denominator of eq 12 with the FFCF evaluated at $T_w = 0$ (eq 5) shows that the CLS is no longer the normalized FFCF once homogeneous broadening is introduced.

However, eq 12 shows that the new CLS decay preserves both the spectral diffusion time constants and the proportionality of the different decay components in the slow spectral diffusion limit. We can also approximate the amplitudes of the parametrized CLS decay from the FFCF parameters

$$\alpha_i = \frac{\Delta_i^2}{(1/T_2)^2 + \sum_j \Delta_j^2} \tag{13}$$

For systems with slow spectral diffusion ($\Delta\tau$ > ~10), α_i were found to correspond to the CLS amplitudes (A_i in eq 9) to within 0.03, which is often within the range of noise and systematic errors that are typical of 2D spectroscopy. This normalized FFCF amplitude will be used as part of the complete algorithmic determination of the FFCF from the CLS.

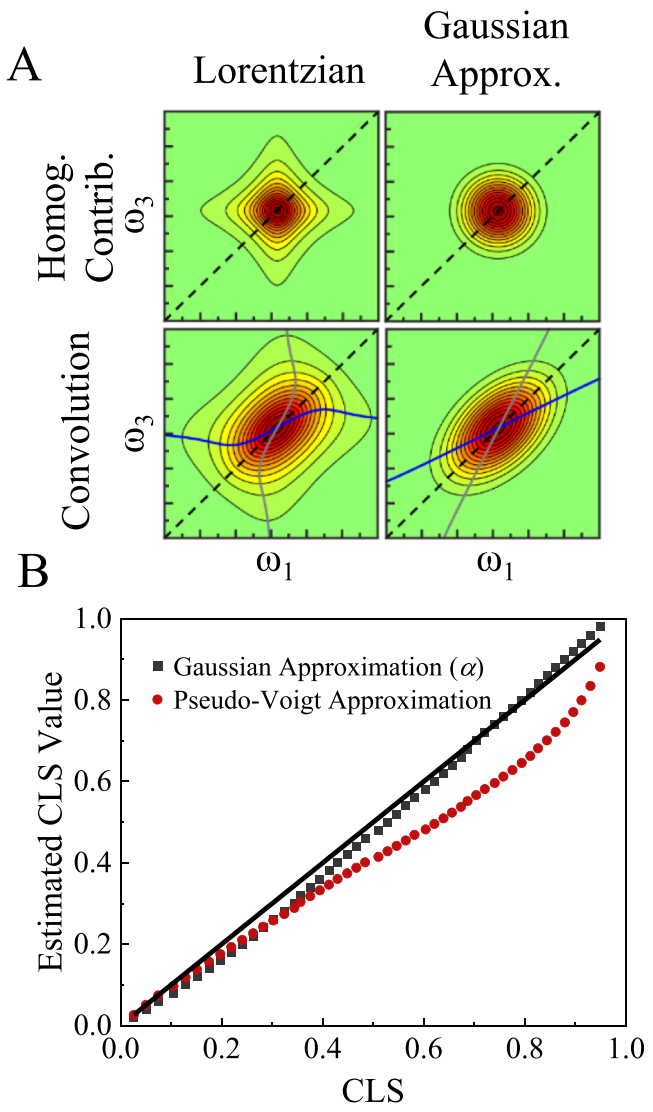

Figure 2. (A) Effect of including a homogeneous component in the FFCF and an illustration of the Gaussian approximation of the homogeneous component. The homogeneous component introduces a 2D Lorentzian component (top left) that is convolved with a correlated Gaussian (e.g., Figure 1A) to yield a 2D Voigt line shape (bottom left). The 2D Lorentzian can be approximated by a Gaussian function of similar size (top right) to get a purely Gaussian convolution with a similar CLS at the center of the line shapes (bottom right). (B) Comparison of the Gaussian approximation given by eq 12 (black points) against the CLS of calculated 2D Voigt line shapes (solid black line). The approximation is of higher quality than the pseudo-Voigt approximation given by the original CLS paper (red points).

https://dx.doi.org/10.1021/acs.jpca.0c04313
J. Phys. Chem. A 2020, 124, 5979−5992

Equation 12 can also be compared against the approximation for the homogeneous contribution given in the original CLS paper based on a 1D pseudo-Voigt approximation:[44]

$$\mathrm{CLS}(T_w = 0) \approx \left(\frac{2.355}{\mathrm{fwhm}}\right)^2 \sum_i \Delta_i^2 \approx 1 - \frac{\Gamma}{\mathrm{fwhm}} \tag{14}$$

where fwhm is the full width at half maximum of the linear line shape as determined from an experimental absorption spectrum or the Fourier transform of eq 4. Equation 14 is plotted as the red points in Figure 2B. While the pseudo-Voigt approximation works well for highly homogeneously broadened lines (CLS < ~0.2), the Gaussian approximation is more accurate across the entire range.

3.3. Partial Motional Narrowing. As was detailed in the original CLS paper, the impact of deviations from the short time approximation on the CLS are very similar to the impact of the homogeneous line.[44] These deviations arise in the case of fast spectral diffusion: when the dimensionless quantity $\Delta\tau$ becomes sufficiently small in eq 6, the first, homogeneous broadening-like term becomes increasingly prominent.[3] This causes the time-domain line shape function to decay slower, creating a non-Gaussian line shape that is narrower than the Gaussian profile predicted in the short-time approximation (eq 7). Physically this phenomenon is interpreted as the frequency of the chromophore fluctuating so fast that it effectively only exhibits an averaged, narrower range of frequencies. Equation 6 also suggests that motional narrowing is either partially or completely converting a Gaussian-like FFCF component into a Lorentzian-like component. This observation correctly indicates that the impact of motional narrowing will reduce the initial correlation of the CLS, as in the case of adding a purely homogeneous line shape component. However, while adding homogeneous broadening makes the line shape broader, motional narrowing will cause the resulting line shape to get narrower. Therefore, it should be possible to distinguish the two contributions based on a combination of the CLS and the fwhm of the absorption spectrum.

The amount of motional narrowing can be heuristically determined for each Kubo line shape component by examining the quantity $\Delta\tau$.[3] This quantity will be denoted $\sigma_i = \Delta_i\tau_i$ for each individual line shape components. Empirically, a line shape component with $\sigma_i < 0.1$ is generally completely motionally narrowed, contributing only a homogeneous component of $1/T_2 = \Delta_i^2\tau_i$. In this case, it can be treated as described in the previous section. A component with $0.1 < \sigma_i < 10$ exhibits partial motional narrowing and contributes both a homogeneous and an inhomogeneous component. A $\sigma_i > 10$ generally is not motionally narrowed and contributes only an inhomogeneous component. As σ_i gets smaller, the CLS amplitude of that component will monotonically decrease.

As in the case with adding in the homogeneous component, the presence of partial motional narrowing can also be empirically shown to preserve the time constants τ_i from the FFCF (eq 5). This effect is shown in Figure 3A. The CLS is plotted for line shapes with FFCFs with two equal amplitude components ($\Delta_1 = \Delta_2 = \Delta$) and time constants $\tau_1 = 1$ ps and $\tau_2 = 10$ ps. The solid lines are fits to the CLS data using eq 9 with the time constants fixed, showing that the time constants are preserved over a wide degree of motional narrowing. These fits also illustrate the utility of parameterizing the FFCF and CLS with the multi-exponential expansion shown in eq 5 and eq 9, respectively. The conservation of the FFCF time constants by the CLS will be a key part of the reconstruction of the FFCF from the CLS in the following section.

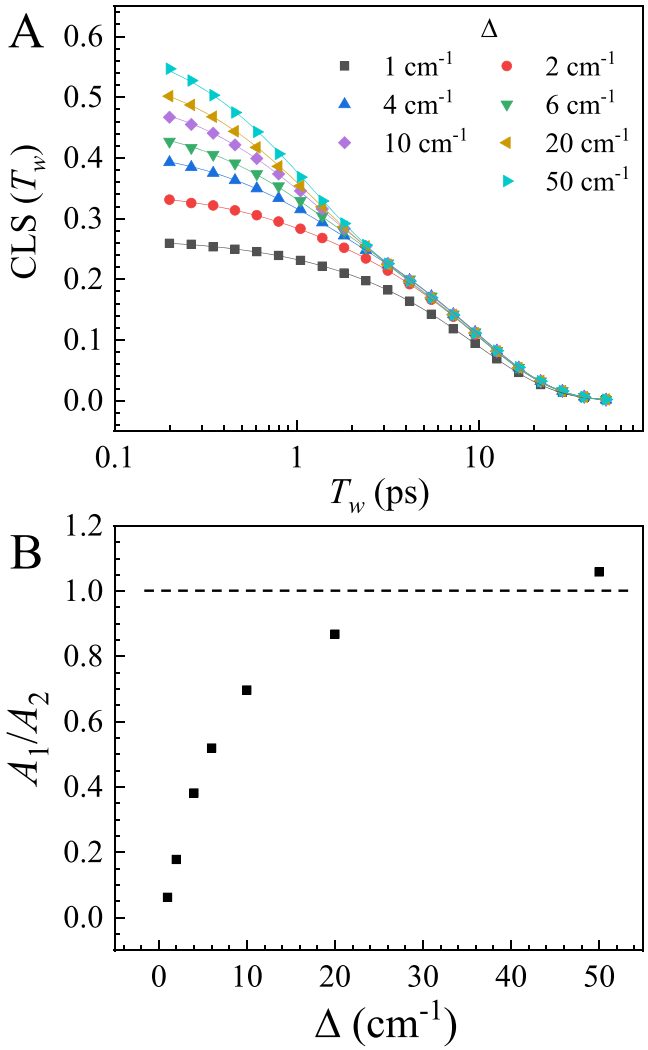

Figure 3. (A) CLS decays from calculated 2D spectra for a range of T_w with FFCFs of the form $C(T_w) = (2\Delta^2)^{1/2}\,\delta(T_w) + \Delta^2 \exp(-T_w/\tau_1) + \Delta^2 \exp(-T_w/\tau_2)$, where $\tau_1 = 1$ ps and $\tau_2 = 10$ ps for variable values of Δ. The solid lines are fits to the equation $\mathrm{CLS}(T_w) = A_1 \exp(-T_w/\tau_1) + A_2 \exp(-T_w/\tau_2)$, where the τ's are held fixed at their FFCF values. The high quality fits demonstrate that motional narrowing will reduce the amplitudes at smaller values of Δ, but the time constants are preserved. (B) Ratio of the CLS amplitudes as a function of Δ. As Δ gets smaller, A_1 gets smaller faster than A_2 because of A_1 becoming increasingly motionally narrowed. The dashed line indicates the proportionality of the FFCF amplitudes.

While the CLS preserves the time constants from the FFCF, the proportionality of the amplitudes of the FFCF are not generally conserved by the CLS amplitudes, A_i. This can be seen immediately by inspection of Figure 3B. Figure 3B shows that the component with the faster dynamics loses more CLS amplitude (A_1) than the slower component (A_2) as Δ decreases. This is a facet of the problem that was not considered in the original FFCF paper, as motional narrowing was only examined in the special case of a one component FFCF in addition to a pure homogeneous component.[44] The amplitude of each individual component get smaller as a function of σ_i. This means that in an FFCF with two spectral diffusion components, a fast spectral diffusion process can have its amplitude heavily

https://dx.doi.org/10.1021/acs.jpca.0c04313
J. Phys. Chem. A 2020, 124, 5979−5992

reduced by motional narrowing, while a slow spectral diffusion process will have minimal motional narrowing and essentially the amplitude predicted by eq 13.

Although the amplitude of a CLS component is highly dependent on the value of its σ_i, it is also not solely dependent upon that value. The magnitude of the effect of motional narrowing on a CLS amplitude is also dependent on the composition of the rest of the line shape. Figure 4 shows the CLS amplitude A_1 of an inhomogeneous component as a function of σ_1 for a set of FFCFs, normalized to the amplitude in the non-motionally narrowed limit (σ_1 goes to ∞). While the amplitude curves have the same general sigmoidal shape with respect to $\log(\sigma_1)$, there are systematic differences between the different FFCFs. If the FFCF has a large motionally narrowed component (black curve in Figure 4), the effect of motional narrowing is suppressed relative to a single component line shape (red curve in Figure 4) for the same value of σ_1. By contrast, if the FFCF has a large, static inhomogeneous component, the effect of motional narrowing will be modestly enhanced (blue curve in Figure 4). The differing degrees of motional narrowing for the different FFCFs with the same value of σ_1 show that the extent of motional narrowing that appears in the CLS is dependent on the entire FFCF. Therefore, there cannot be a highly accurate solution for constructing the FFCF from the CLS or vice-versa that does not account for the entire line shape.

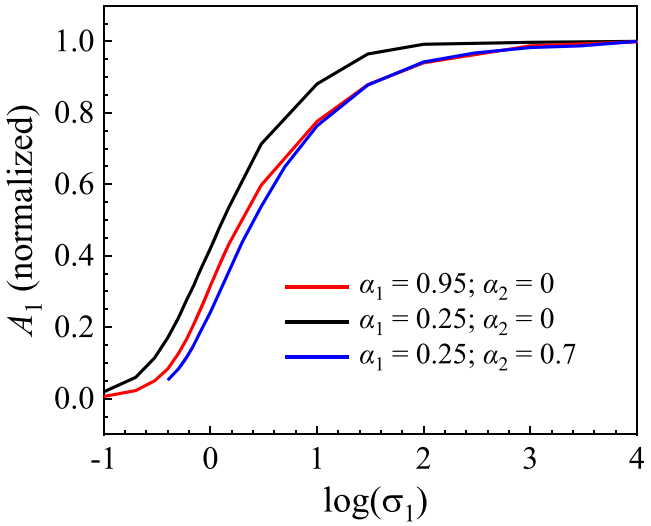

Figure 4. CLS amplitudes, A_1, of a partially motionally narrowed FFCF component for three different FFCFs as a function of the motional narrowing parameter $\sigma_1 = \Delta_1\tau_1$. The curves are normalized to the value of the CLS amplitude in the non-motionally narrowed limit (σ_1 goes to ∞). All three curves have a sigmoidal shape, but there are notable differences between them, indicating that the degree of motional narrowing exhibited depends on the entire FFCF. A large homogeneous component (black curve) will suppress the effect of motional narrowing compared to a small homogeneous component (red curve), while a large static inhomogeneous component (blue curve) will enhance the effect of motional narrowing.

4. DETERMINING THE FFCF FROM THE CLS

4.1. Reducing the Parameter Space. The ultimate goal of this section is to take the parametrized CLS decay that is the observable for the experiment, and use it to obtain the correct FFCF, which is input into the response function equations to calculate experimentally measured linear and 2D line shapes. As was shown in Figure 4, to accurately reconstruct the FFCF from the CLS in the case of partial motional narrowing, the entire CLS has to be considered. In other words, the function to go from a CLS amplitude to an FFCF amplitude does not only depend on that CLS amplitude and its associated time constant, but also on every other CLS amplitude and time constant. To make a complete empirical characterization of the FFCF parameter space feasible, new parameters are introduced that capture the fundamental relationships between the FFCF and CLS decays.

As described in Section 3.2, a useful normalization of the FFCF amplitudes can be found using a Gaussian approximation of the 2D Voigt line shape. The rescaled amplitudes of the FFCF are given by the α_i in eq 13. In the non-motionally narrowed limit, the rescaled FFCF amplitude α_i were shown to be a very good approximation for the CLS amplitudes A_i. As was shown in Section 3.3, this approximation breaks down dramatically in the presence of motional narrowing. However, using the normalized FFCF amplitudes α_i allows an infinite set of FFCFs to be associated with a single CLS curve. The "family" of FFCFs with the same α_i's and τ_i's will give the same CLS per eq 12, as long as none of the components of the CLS are motionally narrowed. The normalization of the FFCF amplitudes also reduces the number of FFCF parameters that need to be sampled by one and restricts each amplitude to a range between zero and one.

Accounting for motional narrowing is again more complicated, as the degree of motional narrowing depends both on the total size of the line shape (through Δ) and the time scale of the decay (through τ). Because of motional narrowing, FFCF families with the same α_i's and τ_i's will have differing CLS amplitudes (if the Δ_i are sufficiently small) because of differences in the corresponding motional narrowing terms, $\sigma_i = \Delta_i\tau_i$. As the Δ_i's are already determined by α_i's, the best way to prevent the degree of motional narrowing from changing within an FFCF family is to then scale the associated time constants. By rescaling the time constants τ to preserve each $\sigma_i = \Delta_i\tau_i$, the amplitudes of the associated CLS decay are then also conserved. This indicates that σ_i is the appropriate conserved dimensionless time scale-like quantity for the family of FFCFs, which are now defined by the FFCFs with the same α_i's and σ_i's. In other words, each set of FFCFs is uniquely described by the normalized amplitude and degree of motional narrowing for each inhomogeneous component.

The above transformation conserves the ratios between different time constants but scales the time axis. As the purpose of these rescalings is to find the set of FFCFs that yielded the same CLS component amplitudes A_i and a set ratio between the time constants τ_i, the family of FFCFs (as defined by α_i and σ_i) should then be related to an associated CLS master curve once each individual CLS curve's time axis is scaled by an appropriate factor. As the FFCF time scale was rescaled by spectral line widths, a sensible choice for this scaling factor is the fwhm of the linear absorption spectrum (which can also be derived from the Fourier transform of eq 4). An experimental CLS curve's time domain can be multiplied by the experimental fwhm of the linear line shape to generate the CLS master curve. An analogous conserved quantity to σ_i can be derived for the CLS by then dividing the fwhm into fractions corresponding to the square root of amplitude terms (creating a Δ_i-like term), and multiplying by the corresponding CLS time constant

$$s_i = \text{fwhm} \cdot \left(A_i / \sum_j A_j \right)^{1/2} \tau_i \tag{15}$$

https://dx.doi.org/10.1021/acs.jpca.0c04313
J. Phys. Chem. A 2020, 124, 5979−5992

Table 1. Rescaled FFCF and CLS Parameters[a]

parameter	FFCF	CLS
amplitude	$\alpha_i = \frac{\Delta_i^2}{(1/T_2)^2 + \sum_j \Delta_j^2}$	A_i
time scale (motional narrowing)	$\sigma_i = \Delta_i \tau_i$	$s_i = \text{fwhm} \cdot \left(A_i / \sum_j A_j \right)^{1/2} \tau_i$
time scale (Gaussian limit)[b]	$\sigma_\infty = 8 \ln(2) \frac{\Delta_i^2}{(\text{fwhm})^2}$	

[a]New FFCF parameters based on FFCF parameters defined in eq 5. New CLS parameters based on CLS parameters in eq 9. fwhm is of the linear 1D line shape. [b]Used in the algorithmic determination of the FFCF from the CLS, not for describing the FFCF parameter space.

Similar to the FFCF α_i terms and the CLS A_i terms, the σ_i and s_i terms scale roughly linearly with each other in the non-motionally narrowed limit, but this simple relationship is again strongly broken in the presence of motional narrowing.

These rescalings reduce the number of parameters in each FFCF family to two for each inhomogeneous component, matching the number of parameters in the rescaled CLS decay. These are split into amplitude-like (α_i and A_i) and time-like (σ_i and s_i) components (see Table 1). By rescaling both the frequency amplitudes and the time constants in this manner, a single rescaled CLS curve can then be related to a large family of FFCFs, which are then only distinguished by the fwhm of the linear spectrum. Figure 5 shows three separate CLS master curves for three different FFCF families over several orders of magnitude of spectral widths, illustrating that these new parameters work as intended. It is important to recognize that these sets of parameters are not equalities, but functional mappings. In other words, the α_i and σ_i can be thought of as single-valued multidimensional functions of all the A_i and s_i, for example, $\alpha_1 = f(A_1, A_2, \ldots; s_1, s_2, \ldots)$. The reverse is also true: the parameters A_i and s_i are functions of the FFCF α_i and σ_i parameters.

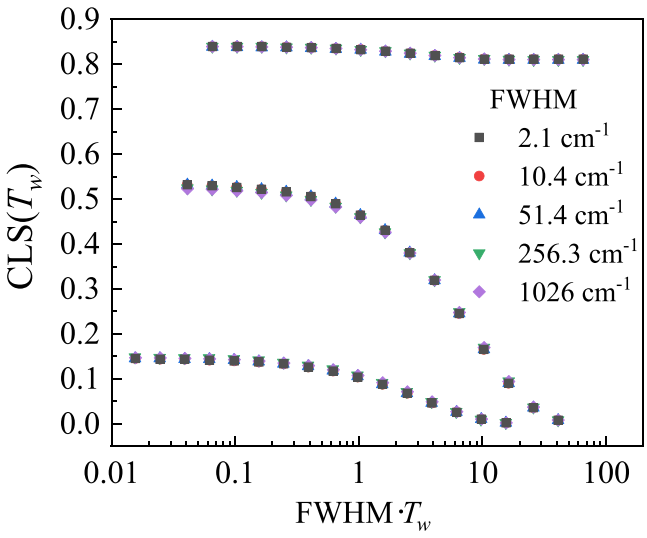

Figure 5. Rescaled CLS decays for three different FFCF families. Each curve is related to a group of FFCFs that have the same rescaled α and σ parameters but varying spectral widths. Scaling the time axis by the spectral width yields a single CLS master curve for each FFCF family. The resulting CLS master curves show that a rescaled CLS can then be related to a rescaled FFCF, which can be distinguished from other FFCFs in its family by the measured spectral width.

4.2. Approximating Functions that Return the FFCF Parameters with Neural Networks. For the purpose of determining the FFCF from the CLS, we are interested in defining functions that take in the CLS parameters A_i and the rescaled s_i as inputs and returning an FFCF parameter (α_i or σ_i). As there is no known analytic treatment available for evaluating these functions, the best approach is to find a high quality empirical approximation that is capable of describing the entire domain of input CLS parameters.

This problem has characteristics that make it amenable to solving using ANNs. A simple feedforward ANN with one hidden layer of neurons is capable of approximating continuous, single valued functions defined on compact subsets of input variables to arbitrary precision.[51,52] Additionally, no knowledge is required of the underlying functional form of the approximated function. Therefore, if sufficiently dense and high quality training data can be applied to training a neural network of this form, the resulting network can be used as a fast and highly accurate approximation of the underlying true function. The problem of determining the underlying function is then reduced to generating a large and representative data set to use to train the neural networks.

To generate the training data sets, 2D line shapes were first calculated for the entire physical range of FFCF parameters. The amplitude-like components, α_i, can vary from 0 to 1, and their sums must be ≤ 1. The time-like components, σ_i, have no upper bound, but have an empirical lower bound of order 0.1, upon which the line shape becomes completely motionally narrowed. In the large σ_i limit motional narrowing is no longer a concern, and other approaches (such as the Gaussian approximation demonstrated in Section 3) can be employed, so a maximum value of $\log(\sigma) \sim 4-8$ was considered, depending on the line shape component. A five parameter model (with three α's and two σ's) corresponding to at most a biexponential FFCF to an offset was chosen as a sufficiently complicated representative system. While preparing a neural network can be done in principle for any number of parameters, as the number of parameters becomes larger, the size of the parameter space and corresponding neural network greatly increases, and similarly the length of time required to train the network also increases. As will be shown later, the networks trained from this data set could be well generalized to a triexponential decay to an offset case without further modification, and are likely further generalizable.

In the case of a static inhomogeneous component (where τ is effectively infinite) or in the case of a very large σ that falls

https://dx.doi.org/10.1021/acs.jpca.0c04313
J. Phys. Chem. A 2020, 124, 5979−5992

outside the domain of the simulated parameter space, it will also be useful to define an alternative version of σ

$$\sigma_\infty = 8\ln(2)\frac{\Delta_i^2}{(\text{fwhm})^2} \tag{16}$$

Like the normal σ parameters, this definition will enable unique determination of the corresponding Δ without requiring accurate knowledge of all of the other FFCF amplitudes or the homogeneous component, as would be required from the definition of an α parameter. This feature will be of use in constructing the FFCF from the neural network outputs. For the training data, the fwhm was determined for an arbitrary FFCF by Fourier transforming the 1D response function (eq 4) to retrieve the 1D line shape. There is no corresponding s_∞, but the σ_∞ parameter is dependent on all of the other A and s parameters.

To characterize the complete range of parameters for a biexponential FFCF with a static inhomogeneous component, 250,000 sets of line shapes were generated. For each set of 2D line shapes, the CLS was then calculated and used to construct the corresponding CLS parameters. To avoid the effects of nonlinearity in the center line in highly homogeneous or motionally narrowed spectra (e.g., Figure 2A, bottom left), the center line's range was limited to a quarter of the linear fwhm on either side of the center frequency. As the FFCF's were made up of three inhomogeneous components, it was found to be sufficient to calculate the CLS at three waiting times for each FFCF: t_1 for the fast decay, t_2 for the slow decay, and t_3 for the static inhomogeneity. The amplitudes of the three CLS components can be found through simple algebraic manipulation

$$\begin{aligned} A_3 &= \text{CLS}(t_3) \\ A_2 &= (\text{CLS}(t_2) - A_3)/\exp(-t_2/\tau_2) \\ A_1 &= (\text{CLS}(t_1) - A_2\exp(-t_1/\tau_2) - A_3)/\exp(-t_1/\tau_1) \end{aligned} \tag{17}$$

for $t_3 \gg \tau_2$, $\tau_2 > t_2 \gg \tau_1$, and $\tau_1 > t_1$. This strong separation of time scales was used to generate the greatest number of CLS parameters from the fewest calculated 2D spectra. It is worth stressing that this condition is not assumed by the algorithm, and the resulting networks were found to perform equally well with relatively small separation of time scales. Using the amplitudes and the time constants from the FFCF as well as the calculated fwhm of the absorption spectra, the rescaled CLS parameters can be calculated (Table 1) for all 250,000 FFCF's. The rescaled CLS parameters can then be related to the original rescaled FFCF parameters.

An example of calculated mappings between these CLS and FFCF parameters can be seen in Figure 6 for the special case of a single inhomogeneous component (one α and one σ parameter). As seen in the plots, the values of α and σ have a roughly linear dependence on A and s, respectively, when the value of s is large (non-motionally narrowed limit). As the value of s gets smaller, the dependencies of both FFCF parameters become nonlinear. However, knowledge of A and s still determine a unique pair of α and σ parameters, which, with knowledge of the experimental time constant, give the unknown FFCF parameters (Δ and T_2). Additionally, the large empty quadrant in the upper left of each panel corresponds to CLS component amplitudes that are not obtainable for a given degree of motional narrowing and correspond to nonphysical FFCFs.

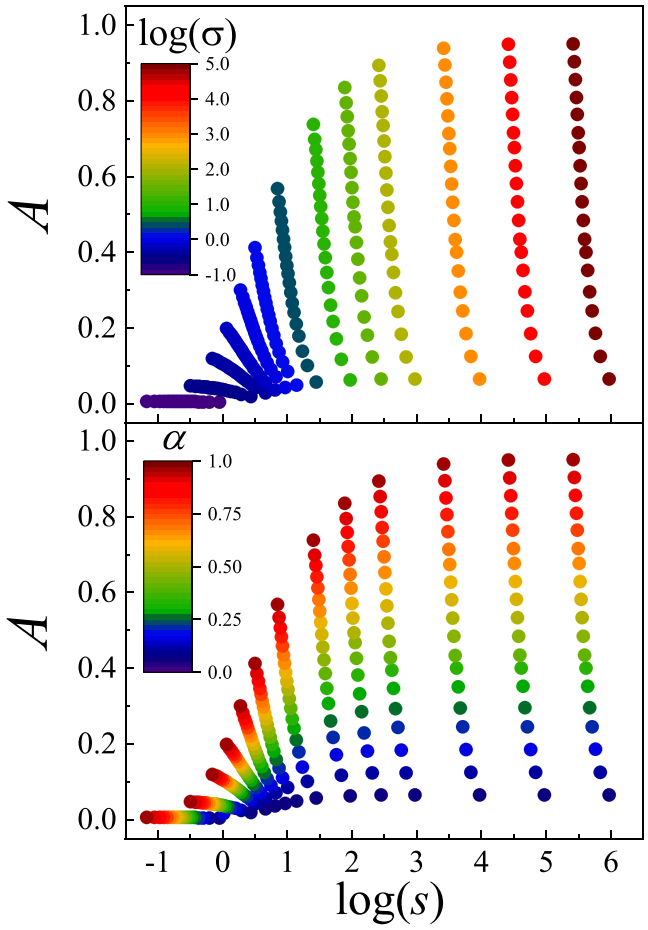

Figure 6. Parameter maps relating the rescaled CLS parameters A and s to the rescaled FFCF parameters α and σ for the case of a single inhomogeneous component FFCF. In the non-motionally narrowed limit (large s) it can be seen that the amplitude-like and time-like parameters are mainly independent of each other, but the dependency becomes highly nonlinear in the motionally narrowed limit. The empty section in the top left of both plots indicate CLS parameters that do not correspond to physical FFCFs due to the effects of motional narrowing. Once the rescaled CLS parameters are used to find the rescaled FFCF parameters, the full FFCF can be determined from knowledge of the CLS time constants.

The training of the neural networks was performed after the training data sets relating the rescaled CLS parameters to the rescaled FFCF parameters were calculated. The neural networks were developed using MATLAB's Neural Network Fitting Application, which was found to be sufficiently powerful for the task. The network structure comprised 5 input neurons corresponding to the 5 rescaled CLS parameters, an output neuron corresponding to a rescaled FFCF parameter, and a variable number of neurons (20−50) in the hidden layer. Each input neuron is connected to all of the hidden neurons, and all of the hidden neurons are connected to the output neuron. Each neuron also has a bias value. Overall, this results in $7n + 1$ fitting parameters for n hidden neurons, as well as 12 parameters connecting the input and output layers to the measured properties. Each neuron's output depends on its inputs, bias, and an activation function

$$y_i = f\left(b_i + \sum_j M_{ij}x_j\right) \tag{18}$$

https://dx.doi.org/10.1021/acs.jpca.0c04313
J. Phys. Chem. A 2020, 124, 5979−5992

where y_i is the output value of a neuron, b_i is the neuron bias, x_j is an input value from the previous layer, and M_{ij} is the weight for that input. For the hidden neurons, the activation function is the hyperbolic tangent function, $f(x) = \tanh(x)$. The output neuron uses a linear activation function, $f(x) = x$.

The 250,000 separate data sets were randomly divided into 70% training, 15% validation, and 15% testing populations and the network was trained using the Levenberg−Marquardt algorithm. After training, each of the three σ neural networks calculated had regressions with R values of at least 0.9998, indicating extremely high correlation. Regressions of the output of the ANN's approximating σ_1, σ_2, and σ_∞ against the calculated parameters are plotted in Figure 7. The regressions for the

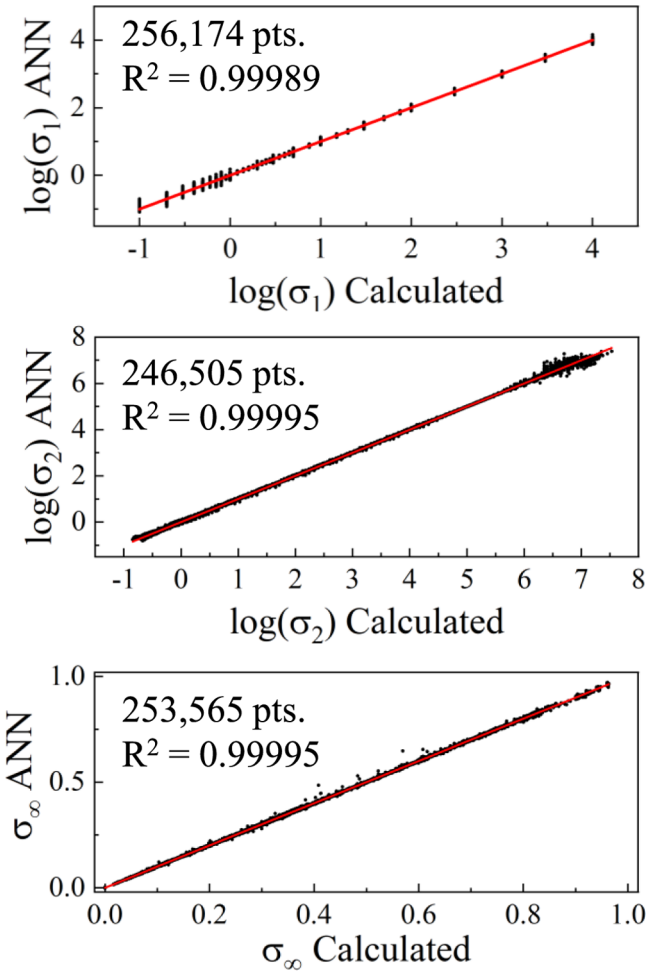

Figure 7. Regressions of the outputs of the artificial neural networks against the calculated FFCF σ parameters defined in the text. The regressions include the data used in the training, validation, and testing populations, all of which have virtually identical statistics. All three networks were able to produce high quality values for the relevant rescaled FFCF parameter as a function of the rescaled CLS parameters.

separate training, validation, and testing populations had nearly identical statistics. Complete tables of weights and biases for the three networks can be found in the Supporting Information. As there is minimal noise (only computational errors) in the underlying training data, there is little concern for overfitting. The results of analogous ANN's for the α parameters were found to be of somewhat lower quality. This could be due to the fact that the α parameters depend on all of the underlying Δ's and the homogeneous component T_2, while the σ parameters only depend on a single Δ. As all of the Δ's can be calculated from the σ's alone (because all of the τ's and the fwhm are experimentally known), the α parameters are only necessary for determining the homogeneous component. An alternative strategy for determining the homogeneous component without calculating an α_i parameter will be discussed in the next section.

4.3. The Complete Algorithm and Generalizing to More FFCF Components. With the working neural networks, a complete algorithm for determining the FFCF from the CLS and the fwhm of the linear spectrum can be developed. First, the rescaled CLS parameters are calculated based on the experimentally determined CLS parameters and the experimentally determined fwhm. The rescaled CLS parameters are used as input parameters for the ANNs to recover the rescaled FFCF parameters, σ_i, with a high degree of accuracy. From the calculated σ's and the experimentally determined τ's from the CLS, the Δ's of the FFCF can then be determined. The only remaining term to be solved for is then the homogeneous component, T_2.

If all of the Δ's are known, this could in principle be done by using a neural network that evaluated an α parameter. This method of determining both α and σ works extremely well in the single inhomogeneous component case that was shown in Figure 6, and can be in principle generalized to an arbitrary number of components. However, the resulting neural networks were found to be of relatively low quality compared to those for the σ parameters. An alternative strategy was employed for determining the complete FFCF after the Δ's were determined. From here, the 1D response function (eq 4) is calculated for an FFCF with the known Δ's and τ's, but with an arbitrary value for the homogeneous line. The calculated response function is then numerically Fourier transformed to yield the linear line shape for the FFCF given by the set of Δ_i and τ_i and the arbitrary T_2. The value of T_2 is then varied until the fwhm of the calculated line shape matches the fwhm of the experimental line shape. As the problem is reduced to a 1D function minimization that is free from false local minima, this calculation can be performed extremely quickly, although not as quickly as the ANN calculations. In practice, it also provides an additional quality check, as there will be no solution if the calculated FFCF is nonphysical (i.e., in the empty space in the top left of the parameter maps in Figure 6), and provides an advantage over more traditional iterative approaches for determining the FFCF from the CLS. This manifests as the linewidth calculated for the FFCF with $1/T_2$ set to zero being larger than the experimental linewidth.

Although many CLS decays can be described with a biexponential decay to an offset, complicated chemical systems can often have decays with more time scales. While the most natural way to approach this problem is to add yet more parameters to the neural network, the biexponential neural networks can be easily generalized to accommodate triexponential decays. The parameters for a triexponential can be constructed from the previously trained neural networks

$$\sigma_1 = f_1(A_1, s_1, A_2, s_2, A_3 + A_4)$$
$$\sigma_2 = f_2(A_1, s_1, A_2, s_2, A_3 + A_4)$$
$$\sigma_3 = f_2(A_1 + A_2, \sqrt{s_1 s_2}, A_3, s_3, A_4)$$
$$\sigma_\infty = f_\infty(A_1, s_1, A_2 + A_3, \sqrt{s_2 s_3}, A_4) \quad (19)$$

https://dx.doi.org/10.1021/acs.jpca.0c04313
J. Phys. Chem. A 2020, 124, 5979−5992

where f_i corresponds to the neural network function relating to σ_i for the biexponential to an offset case described in the previous section. In short, it groups the slowest components together as a static offset for the determination of the first two components, groups the fastest components together for determining the third component, and groups the second and third components together for determining the offset. This parameterization is effective for a wide range of time scales, including when the third component exhibits partial motional narrowing. It is likely that tetraexponentials or more could be accommodated in an analogous fashion. Fortunately, increasing the number of resolvable exponentials requires a large separation of time scales between the fastest and slowest exponentials, and requires a non-negligible amplitude for all components. As the range of time scales and frequency amplitudes that 2D CS can measure rarely span more than a few orders of magnitude, both of these requirements reduce the possibility for requiring additional FFCF components to characterize experimental data. As each σ still uniquely identifies a corresponding Δ, the homogeneous line width can be determined from the calculation of the 1D line shape as before.

The complete algorithm will also be available as a standalone piece of software (CAFE) that is available free for download at the URL provided in the ref 50. The software provides an intuitive GUI based on the MATLAB GUIDE package and runs on the freely available MATLAB 2014b 64-bit run time environment. The software additionally calculates 1D and 2D spectra based on the FFCF parameters, which provide additional quality checks by comparison to experimental data.

5. EXAMPLE APPLICATIONS

5.1. Experimental 2D IR Data. To demonstrate the robustness of the algorithm, two examples from previously reported 2D IR experiments are presented. The first data set that will be considered is methylthiocyanate (MeSCN) in H_2O.[53] As has been previously reported, the CLS decay for MeSCN in H_2O gives the same time constants as has been previously seen by other probe molecules.[53] However, MeSCN has a dramatically narrower line width than previously used probes, such as HOD.[6] This narrow line width combined with the fast dynamics of water results in a large degree of motional narrowing of both FFCF components. The computed rescaled CLS terms $\log(s_1)$ and $\log(s_2)$ are approximately −0.22 and +0.36, respectively. As seen in Figure 6, this corresponds to an extreme degree of motional narrowing in both components. Despite these strong nonlinearities, the neural network algorithm is capable of producing an FFCF that produces 2D line shapes with the correct CLS and the correct 1D line shape (Figure 8A). As seen by the significant deviations from the Gaussian approximation (blue curve in Figiure 8A, corresponding to eq 12) and the prominent wings in the 1D spectra, the algorithm can give the correct results even far from the Gaussian limits that were used in the original CLS papers.

The second data set that will be considered is for phenylselenocyanate (PhSeCN) in supercooled benzophenone (BZP).[54] PhSeCN is a vibrational probe with a very long lifetime that enables multiple decades of 2D spectra to be collected, and supercooled liquids are known to have decays with complicated functional forms. At 270 K, the experimental CLS decay requires three exponential components to fit it. Using the modified equations given in eq 19, the algorithm can give an accurate result for this functional form that was not explicitly part of the training data set (Figure 8B). This is true even when the fastest

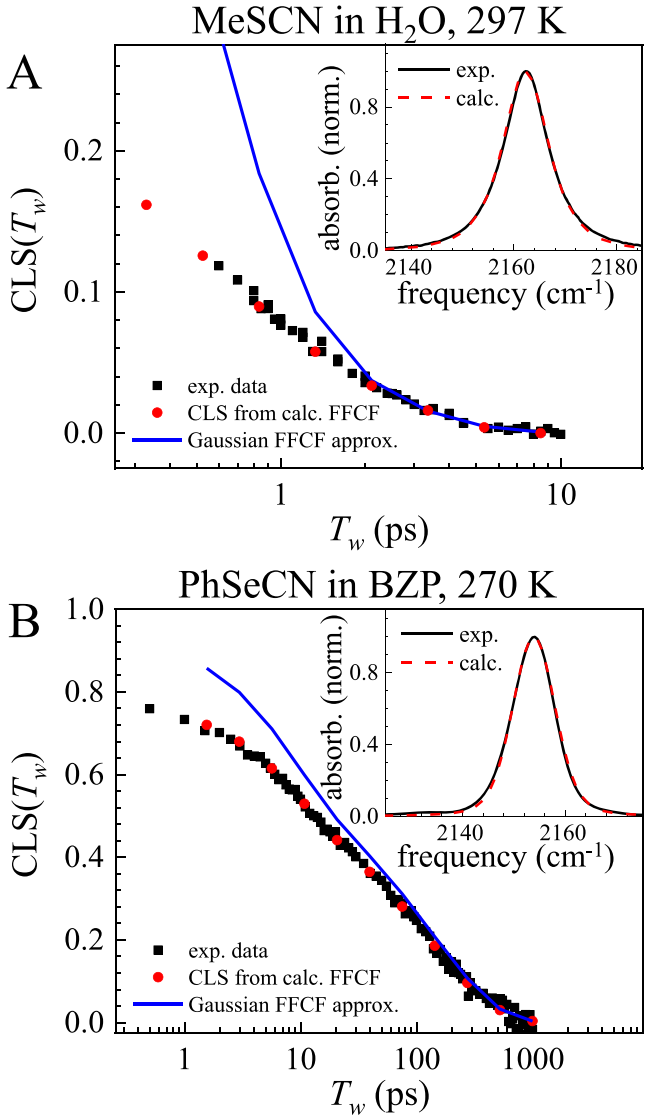

Figure 8. CLS neural network algorithm applied to 2D IR and Fourier transform infrared (FTIR) data. Black points are experimental CLS data, red points are derived from the CLS of 2D spectra generated from the calculated FFCF, and blue curves are the Gaussian approximation to the FFCF (eq 12). (A) MeSCN in H_2O data[53] has two components that have different degrees of partial motional narrowing. The fast component is highly motionally narrowed, as demonstrated by the massive deviations from the Gaussian approximation. The calculated 1D absorption spectrum (inset), which displays Lorentzian-like wings, captures the highly non-Gaussian behavior of the experimental FTIR spectrum. (B) PhSeCN in BZP data[54] has three exponential decays and partial motional narrowing, illustrating the ability of the neural networks to describe triexponential decays (eq 19). The calculated 1D absorption spectrum (inset) captures the more Gaussian-like character of the FTIR spectrum.

dynamics exhibit some degree of motional narrowing ($\log(s_1)$ = 0.92). It can be seen that the FFCF returned by the algorithm also gives the correct 1D line shape (Figure 8B inset), which is much more Gaussian than that of MeSCN in H_2O.

5.2. Polarization-Dependent Motional Narrowing from RISD. The degree of motional narrowing exhibited by a probe molecule in a 2D experiment can also depend on the polarizations of light used in the measurements. RISD relates polarization-dependent spectral diffusion to a combination of

https://dx.doi.org/10.1021/acs.jpca.0c04313
J. Phys. Chem. A 2020, 124, 5979−5992

the solvent's structural fluctuations and the reorientation of the probe molecule, which can cause spectral diffusion through the Stark effect.[43] All of the polarization-dependent RISD components are determined from separate measurements of the probe's orientational relaxation made with polarization selective pump−probe experiments.[43] The effects of RISD cause the perpendicularly polarized FFCF ("XXYY") to become faster than the parallel FFCF ("XXXX"). The perpendicular polarization can experience a greater degree of motional narrowing than the parallel polarization because of its faster dynamics. Correctly compensating for this differing degree of motional narrowing provides an independent quality check on the FFCFs computed with this algorithm.

The RISD effect is shown in Figure 9, which reexamines data taken on KSeCN in 1-methylimidazole (1-MeIm) from a previous publication.[55] This system should be well described by the RISD equations as 1-MeIm is a simple liquid without strong chemical interactions with the KSeCN probe. The best fit to the CLS data using the RISD equations in Figure 9A systematically misses both the parallel and perpendicular data. When the CLS is used in the data analysis rather than the FFCFs, the faster FFCF decay (perpendicular) causes more extensive partial motional narrowing, making the difference between the parallel and perpendicular CLS decays greater. The result is that the best simultaneous fit to the parallel and perpendicular CLS data is forced to be too slow for perpendicular and too fast for parallel (Figure 9A). However, if the parallel and perpendicular CLS curves are each converted to their corresponding FFCFs, these FFCFs can then be simultaneously fit using the RISD equations with the SSD parameters adjustable. The results of this procedure are shown in Figure 9B. The fit matches the parallel and perpendicular curves exceedingly well. This provides validation for both RISD and for the algorithmic determination of the FFCF that is independent of the tests used in Figure 8. Figure 9 also shows that deviations from theoretical descriptions of the FFCF can occur from analyzing the CLS rather than the FFCF.

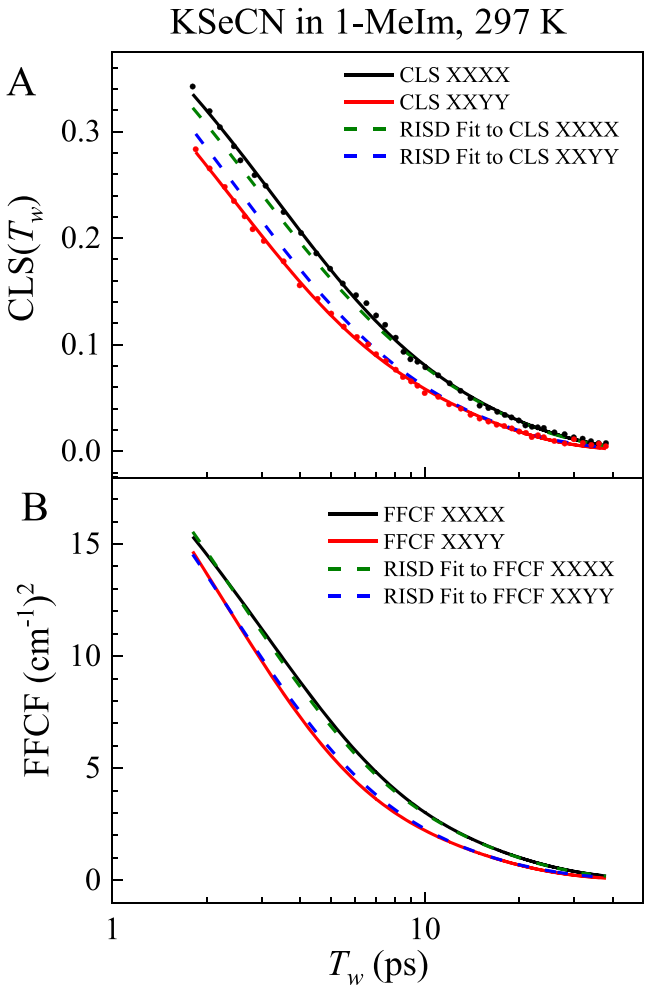

Figure 9. Illustration of polarization-dependent motional narrowing from RISD for experimental data from the CN stretching mode in the sample, KSeCN in 1-MeIm.[55] Because of RISD, the perpendicular XXYY polarization has faster dynamics than the parallel XXXX polarization, causing a greater degree of motional narrowing in the XXYY case. The differences in motional narrowing cause systematic deviations when RISD fits are applied to the CLS decays (top). By contrast, the RISD fits to the calculated FFCF (bottom) derived from each CLS decay are almost quantitatively accurate.

5.3. Motional Narrowing with Stokes Shift and Underdamped Oscillations. Finally, it is necessary to examine how deviation from the classical FFCF, which describes high temperature, weak coupling, and low frequency bath modes, affects the extent of motional narrowing.[33,48] While these classical conditions are usually applicable in 2D IR spectroscopy, they are more likely to be violated in 2D ES experiments.[48] In particular, two limiting cases of the quantum FFCF components are important in 2D ES: the overdamped FFCF component (responsible for both spectral diffusion and Stokes shift) and the underdamped FFCF component (oscillations from high frequency coupling, such as in vibronic coupling). These particular cases have been previously shown to give the correct CLS ω_3 in the non-motionally narrowed limit.[48]

To examine the impacts of these nonclassical effects on the CLS of a motionally narrowed line shape, they were introduced into an FFCF based on the MeSCN in H_2O FFCF shown in Figure 8A. Details of the calculations can be found in the Supporting Information. Introducing a new, underdamped FFCF component results in an oscillatory signal in the CLS (Figure 10, red curve). However, the oscillations are evenly distributed around the classical FFCF components (Figure 10 black curve), demonstrating that including an underdamped component does not change the degree of motional narrowing in the diffusive part of the FFCF, which can then be accurately extracted.

To implement the Stokes shift, a high temperature limit ($kT > \hbar/\tau$) of the overdamped FFCF component was used.[33] Within this limit, the magnitude of the Stokes shift (and coupling strength), λ, is related to the linewidth by[33,48]

$$\Delta^2 = \frac{2\lambda kT}{\hbar} \tag{20}$$

This interplay between temperature, relaxation rate, frequency amplitude, and Stokes shift amplitude also gives an inequality that must hold within the temperature condition

$$\Delta\sigma > 2\lambda \tag{21}$$

where $\sigma = \Delta\tau$ as before. This illustrates that the maximum Stokes shift possible (in units of Δ) within this limit is proportional to the degree of motional narrowing. Using the high temperature condition with eq 20, for the model FFCF chosen the lowest temperature that can be considered is ~20 K, and the largest magnitude Stokes shift is ~0.3 Δ_1. In this case, the CLS (Figure 10, blue points) is indistinguishable from the classical FFCF. As

https://dx.doi.org/10.1021/acs.jpca.0c04313
J. Phys. Chem. A 2020, 124, 5979−5992

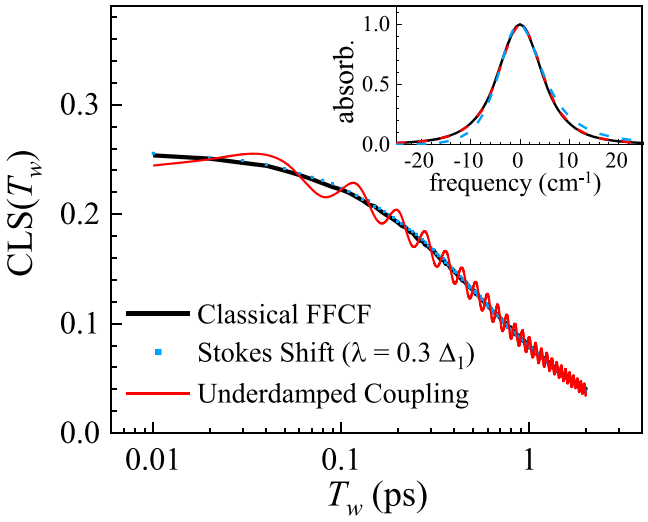

Figure 10. Comparison of CLS decays with quantum FFCFs illustrating phenomena common to 2D electronic spectroscopy on a log plot. The diffusive parts of the FFCF in all cases are the same as in Figure 8A, and are substantially motionally narrowed. Black curve: classical FFCF identical to that shown in Figure 8A. Blue points: overdamped FFCF components demonstrating a Stokes shift. The largest Stokes shift was used that still satisfies the high temperature condition (see text). The CLS is virtually identical to the classical case. Red curve: The FFCF includes an underdamped component (e.g., high frequency coupling). The oscillations are distributed around the classical CLS. Inset: Absorption spectra for all three cases, demonstrating that the fwhm has not changed.

none of these modifications change the absorption spectrum's fwhm (Figure 10, inset), the algorithm for retrieving the real valued, diffusive part of the FFCF from the CLS and absorption fwhm still holds. While this analysis does not exhaustively cover all coupling strengths and temperature regimes, it shows that the procedures developed here should be broadly applicable to diffusive Gaussian dynamics in 2D ES and 2D IR spectroscopies.

6. CONCLUSIONS

A new algorithmic approach for quickly and accurately determining the FFCF from experimentally measured CLS data and the fwhm of the linear absorption spectrum was presented. Based on empirical observations on the impact of homogeneous broadening and partial motional narrowing on the CLS observable, a new set of rescaled parameters was developed for both the FFCF and the CLS. These new parameters generate a family of FFCF functions that all yield the same rescaled CLS but give a distinct linear absorption linewidth, which enables the correct FFCF to be determined. These parameters also serve to greatly restrict the parameter space of possible FFCFs by associating many FFCFs with a single rescaled FFCF, which corresponds to a single rescaled CLS master curve.

For the case of an FFCF with the functional form of a biexponential decay to an offset, a large data set of 2D spectra were calculated from over 250,000 distinct FFCF families. For each of the 250,000 cases, the rescaled FFCF parameters were determined and the associated rescaled CLS parameters were numerically derived from the calculated spectra. These parameter mappings were used to train feedforward neural networks to approximate the value of a rescaled FFCF parameter based on the values of the rescaled CLS parameters. The derived neural networks were found to give fast and accurate predictions for the time-like FFCF parameters. By combining these networks with the empirical observation that the CLS preserves the FFCF time constants, the values of each of the inhomogeneous linewidth components can be readily calculated from the rescaled CLS parameters. The remaining homogeneous component of the total absorption line can be quickly calculated by adjusting it until a calculation of the 1D line shape from the response function yields the correct spectral fwhm.

As the CLS observable has grown in popularity as a measure of spectral diffusion because of its robustness, insensitivity to experimental issues (e.g., pulse duration), and ease of calculation, it is important to address any inconsistencies between the observable and the underlying FFCF it can be used to determine. It is important to note that the CLS is a useful observable that provides a great deal of information and that it can be calculated with simulations. However, until now it has not been straightforward to go directly from the experimental CLS to the FFCF except within a limited range of parameters. This work characterizes the behavior of the CLS far from the limiting case that was the basis for the original derivation and provides a method for obtaining the FFCF from the CLS. The rescaled parameters also reflects the deeper phenomenology of the FFCF by describing families of FFCFs that yield the same CLS decay. These phenomenological observations can facilitate deeper understanding of the CLS observable and the nature of motional narrowing in addition to providing the framework for fast algorithmic determination of the FFCF from experimental data.

■ ASSOCIATED CONTENT

Supporting Information

The Supporting Information is available free of charge at https://pubs.acs.org/doi/10.1021/acs.jpca.0c04313.

ANN Parameters as Excel spread sheet(XLSX)

Complete neural network calculations; complete calculations for FFCF Delta parameters; complete calculations for FFCF homogeneous line width; neural network standard error and error propagation from CLS fits; and calculations of a quantum FFCF in various limits (PDF)

■ AUTHOR INFORMATION

Corresponding Author

Michael D. Fayer − *Department of Chemistry, Stanford University, Stanford, California 94305, United States;* orcid.org/0000-0002-0021-1815; Phone: 650 723-4446; Email: fayer@stanford.edu

Author

David J. Hoffman − *Department of Chemistry, Stanford University, Stanford, California 94305, United States;* orcid.org/0000-0001-8518-7676

Complete contact information is available at: https://pubs.acs.org/10.1021/acs.jpca.0c04313

Notes

The authors declare no competing financial interest.

■ ACKNOWLEDGMENTS

This work was supported by the Office of Naval Research by ONR: N00014-17-1-2656.

REFERENCES

(1) Ernst, R. R.; Bodenhausen, G.; Wokaun, A. *Principles of Nuclear Magnetic Resonance in One and Two Dimensions*; Oxford University Press: Oxford, U.K., 1987.

(2) Park, S.; Kwak, K.; Fayer, M. D. Ultrafast 2D-IR vibrational echo spectroscopy: A probe of molecular dynamics. *Laser Phys. Lett.* **2007**, *4*, 704−718.

(3) Hamm, P.; Zanni, M. *Concepts and methods of 2D infrared spectroscopy*; Cambridge University Press, 2011.

(4) Brixner, T.; Mančal, T.; Stiopkin, I. V.; Fleming, G. R. Phase-stabilized two-dimensional electronic spectroscopy. *J. Chem. Phys.* **2004**, *121*, 4221−4236.

(5) Tseng, C.-H.; Matsika, S.; Weinacht, T. C. Two-Dimensional Ultrafast Fourier Transform Spectroscopy in the Deep Ultraviolet. *Opt. Express* **2009**, *17*, 18788.

(6) Asbury, J. B.; Steinel, T.; Stromberg, C.; Corcelli, S. A.; Lawrence, C. P.; Skinner, J. L.; Fayer, M. D. Water Dynamics: Vibrational Echo Correlation Spectroscopy and Comparison to Molecular Dynamics Simulations. *J. Phys. Chem. A* **2004**, *108*, 1107−1119.

(7) Eaves, J. D.; Loparo, J. J.; Fecko, C. J.; Roberts, S. T.; Tokmakoff, A.; Geissler, P. L. Hydrogen bonds in liquid water are broken only fleetingly. *Proc. Nat. Acad. Sci. U.S.A.* **2005**, *102*, 13019−13022.

(8) Kraack, J. P. Ultrafast structural molecular dynamics investigated with 2D infrared spectroscopy methods. *Multidimensional Time-Resolved Spectroscopy*; Springer: Cham, Switzerland, 2019; pp 113−205.

(9) Zheng, J.; Kwak, K.; Asbury, J. B.; Chen, X.; Piletic, I. R.; Fayer, M. D. Ultrafast Dynamics of Solute-Solvent Complexation Observed at Thermal Equilibrium in Real Time. *Science* **2005**, *309*, 1338−1343.

(10) Kim, Y. S.; Hochstrasser, R. M. Chemical exchange 2D IR of hydrogen-bond making and breaking. *Proc. Nat. Acad. Sci. U.S.A.* **2005**, *102*, 11185−11190.

(11) Ji, M.; Odelius, M.; Gaffney, K. J. Large angular jump mechanism observed for hydrogen bond exchange in aqueous perchlorate solution. *Science* **2010**, *328*, 1003−1005.

(12) Yuan, R.; Napoli, J. A.; Yan, C.; Marsalek, O.; Markland, T. E.; Fayer, M. D. Tracking Aqueous Proton Transfer by Two-Dimensional Infrared Spectroscopy and ab Initio Molecular Dynamics Simulations. *ACS Cent. Sci.* **2019**, *5*, 1269−1277.

(13) Kim, Y. S.; Hochstrasser, R. M. Applications of 2D IR spectroscopy to peptides, proteins, and hydrogen-bond dynamics. *J. Phys. Chem. B* **2009**, *113*, 8231−8251.

(14) Ghosh, A.; Ostrander, J. S.; Zanni, M. T. Watching Proteins Wiggle: Mapping Structures with Two-Dimensional Infrared Spectroscopy. *Chem. Rev.* **2017**, *117*, 10726−10759.

(15) Yan, C.; Nishida, J.; Yuan, R.; Fayer, M. D. Water of Hydration Dynamics in Minerals Gypsum and Bassanite: Ultrafast 2D IR Spectroscopy of Rocks. *J. Am. Chem. Soc.* **2016**, *138*, 9694−9703.

(16) Nishida, J.; Breen, J. P.; Lindquist, K. P.; Umeyama, D.; Karunadasa, H. I.; Fayer, M. D. Dynamically Disordered Lattice in a Layered Pb-I-SCN Perovskite Thin Film Probed by Two-Dimensional Infrared Spectroscopy. *J. Am. Chem. Soc.* **2018**, *140*, 9882−9890.

(17) Rosenfeld, D. E.; Gengeliczki, Z.; Smith, B. J.; Stack, T. D. P.; Fayer, M. D. Structural Dynamics of a Catalytic Monolayer Probed by Ultrafast 2D IR Vibrational Echoes. *Science* **2011**, *334*, 634−639.

(18) Zhang, Z.; Piatkowski, L.; Bakker, H. J.; Bonn, M. Ultrafast vibrational energy transfer at the water/air interface revealed by two-dimensional surface vibrational spectroscopy. *Nat. Chem.* **2011**, *3*, 888−893.

(19) Nemeth, A.; Milota, F.; Mančal, T.; Lukeš, V.; Hauer, J.; Kauffmann, H. F.; Sperling, J. Vibrational wave packet induced oscillations in two-dimensional electronic spectra. I. Experiments. *J. Chem. Phys.* **2010**, *132*, 184514.

(20) Richter, J. M.; Branchi, F.; Valduga De Almeida Camargo, F.; Zhao, B.; Friend, R. H.; Cerullo, G.; Deschler, F. Ultrafast carrier thermalization in lead iodide perovskite probed with two-dimensional electronic spectroscopy. *Nat. Commun.* **2017**, *8*, 1−7.

(21) Bakulin, A. A.; Morgan, S. E.; Kehoe, T. B.; Wilson, M. W. B.; Chin, A. W.; Zigmantas, D.; Egorova, D.; Rao, A. Real-time observation of multiexcitonic states in ultrafast singlet fission using coherent 2D electronic spectroscopy. *Nat. Chem.* **2016**, *8*, 16−23.

(22) Caram, J. R.; Zheng, H.; Dahlberg, P. D.; Rolczynski, B. S.; Griffin, G. B.; Dolzhnikov, D. S.; Talapin, D. V.; Engel, G. S. Exploring size and state dynamics in CdSe quantum dots using two-dimensional electronic spectroscopy. *J. Chem. Phys.* **2014**, *140*, 084701.

(23) Stone, K. W.; Gundogdu, K.; Turner, D. B.; Li, X.; Cundiff, S. T.; Nelson, K. A. Two-Quantum 2D FT Electronic GaAs Quantum Wells. *Science* **2009**, *324*, 1169−1173.

(24) Do, T. N.; Khyasudeen, M. F.; Nowakowski, P. J.; Zhang, Z.; Tan, H. S. Measuring Ultrafast Spectral Diffusion and Correlation Dynamics by Two-Dimensional Electronic Spectroscopy. *Chem.—Asian J.* **2019**, *14*, 3992−4000.

(25) Khyasudeen, M. F.; Nowakowski, P. J.; Nguyen, H. L.; Sim, J. H. N.; Do, T. N.; Tan, H.-S. Studying the spectral diffusion dynamics of chlorophyll a and chlorophyll b using two-dimensional electronic spectroscopy. *Chem. Phys.* **2019**, *527*, 110480.

(26) Moca, R.; Meech, S. R.; Heisler, I. A. Two-Dimensional Electronic Spectroscopy of Chlorophyll a: Solvent Dependent Spectral Evolution. *J. Phys. Chem. B* **2015**, *119*, 8623−8630.

(27) Wells, K. L.; Zhang, Z.; Rouxel, J. R.; Tan, H.-S. Measuring the spectral diffusion of Chlorophyll A using two-dimensional electronic spectroscopy. *J. Phys. Chem. B* **2013**, *117*, 2294−2299.

(28) Lewis, N. H. C.; Dong, H.; Oliver, T. A. A.; Fleming, G. R. Measuring correlated electronic and vibrational spectral dynamics using line shapes in two-dimensional electronic-vibrational spectroscopy. *J. Chem. Phys.* **2015**, *142*, 174202.

(29) Courtney, T. L.; Fox, Z. W.; Slenkamp, K. M.; Khalil, M. Two-dimensional vibrational-electronic spectroscopy. *J. Chem. Phys.* **2015**, *143*, 154201.

(30) Singh, P. C.; Inoue, K.-i.; Nihonyanagi, S.; Yamaguchi, S.; Tahara, T. Femtosecond Hydrogen Bond Dynamics of Bulk-like and Bound Water at Positively and Negatively Charged Lipid Interfaces Revealed by 2D HD-VSFG Spectroscopy. *Angew. Chem., Int. Ed.* **2016**, *55*, 10621−10625.

(31) Xiong, W.; Laaser, J. E.; Mehlenbacher, R. D.; Zanni, M. T. Adding a dimension to the infrared spectra of interfaces using heterodyne detected 2D sumfrequency generation (HD 2D SFG) spectroscopy. *Proc. Nat. Acad. Sci. U.S.A.* **2011**, *108*, 20902−20907.

(32) Teo, S. M.; Ofori-Okai, B. K.; Werley, C. A.; Nelson, K. A.; Invited Article. Single-shot THz detection techniques optimized for multidimensional THz spectroscopy. *Rev. Sci. Instrum.* **2015**, *86*, 051301.

(33) Mukamel, S. *Principles of Nonlinear Optical Spectroscopy*; Oxford University Press: Oxford, U.K., 1995.

(34) Nee, M. J.; Baiz, C. R.; Anna, J. M.; McCanne, R.; Kubarych, K. J. Multilevel vibrational coherence transfer and wavepacket dynamics probed with multidimensional IR spectroscopy. *J. Chem. Phys.* **2008**, *129*, 084503.

(35) Khalil, M.; Demirdöven, N.; Tokmakoff, A. Vibrational coherence transfer characterized with Fourier-transform 2D IR spectroscopy. *J. Chem. Phys.* **2004**, *121*, 362−373.

(36) Zheng, J.; Kwak, K.; Xie, J.; Fayer, M. D. Ultrafast Carbon-Carbon Single-Bond Rotational Isomerization in Room-Temperature Solution. *Science* **2006**, *313*, 1951−1955.

(37) Tan, H.-S.; Piletic, I. R.; Fayer, M. D. Polarization selective spectroscopy experiments: methodology and pitfalls. *J. Opt. Soc. Am. B* **2005**, *22*, 2009.

(38) Finkelstein, I. J.; Goj, A.; McClain, B. L.; Massari, A. M.; Merchant, K. A.; Loring, R. F.; Fayer, M. D. Ultrafast dynamics of myoglobin without the distal histidine: Stimulated vibrational echo experiments and molecular dynamics simulations. *J. Phys. Chem. B* **2005**, *109*, 16959−16966.

(39) Kwac, K.; Lee, C.; Jung, Y.; Han, J.; Kwak, K.; Zheng, J.; Fayer, M. D.; Cho, M. Phenol-benzene complexation dynamics: Quantum chemistry calculation, molecular dynamics simulations, and two dimensional IR spectroscopy. *J. Chem. Phys.* **2006**, *125*, 244508.

https://dx.doi.org/10.1021/acs.jpca.0c04313
J. Phys. Chem. A 2020, 124, 5979−5992

(40) Kuroda, D. G.; Vorobyev, D. Y.; Hochstrasser, R. M. Ultrafast relaxation and 2D IR of the aqueous trifluorocarboxylate ion. *J. Chem. Phys.* **2010**, *132*, 044501.
(41) Lee, M. W.; Carr, J. K.; Göllner, M.; Hamm, P.; Meuwly, M. 2D IR spectra of cyanide in water investigated by molecular dynamics simulations. *J. Chem. Phys.* **2013**, *139*, 054506.
(42) Bakker, H. J.; Skinner, J. L. Vibrational spectroscopy as a probe of structure and dynamics in liquid water. *Chem. Rev.* **2010**, *110*, 1498−1517.
(43) Kramer, P. L.; Nishida, J.; Fayer, M. D. Separation of experimental 2D IR frequency-frequency correlation functions into structural and reorientation-induced contributions. *J. Chem. Phys.* **2015**, *143*, 124505.
(44) Kwak, K.; Park, S.; Finkelstein, I. J.; Fayer, M. D. Frequency-frequency correlation functions and apodization in two-dimensional infrared vibrational echo spectroscopy: A new approach. *J. Chem. Phys.* **2007**, *127*, 124503.
(45) Kwak, K.; Rosenfeld, D. E.; Fayer, M. D. Taking apart the two-dimensional infrared vibrational echo spectra: More information and elimination of distortions. *J. Chem. Phys.* **2008**, *128*, 204505.
(46) Roy, S.; Pshenichnikov, M. S.; Jansen, T. L. C. Analysis of 2D CS spectra for systems with non-gaussian dynamics. *J. Phys. Chem. B* **2011**, *115*, 5434−5440.
(47) Fenn, E. E.; Fayer, M. D. Extracting 2D IR frequency-frequency correlation functions from two component systems. *J. Chem. Phys.* **2011**, *135*, 074502.
(48) Šanda, F.; Perlík, V.; Lincoln, C. N.; Hauer, J. Center Line Slope Analysis in Two-Dimensional Electronic Spectroscopy. *J. Phys. Chem. A* **2015**, *119*, 10893−10909.
(49) Nowakowski, P. J.; Khyasudeen, M. F.; Tan, H.-S. The effect of laser pulse bandwidth on the measurement of the frequency fluctuation correlation functions in 2D electronic spectroscopy. *Chem. Phys.* **2018**, *515*, 214−220.
(50) https://web.stanford.edu/group/fayer/CAFE.html (Accessed May 12, 2020).
(51) Debao, C. Degree of approximation by superpositions of a sigmoidal function. *Approx. Theor. Appl.* **1993**, *9*, 17−28.
(52) Hassoun, M. H. *Fundamentals of Artificial Neural Networks*; MIT Press: Cambridge, MA, 1995.
(53) Yuan, R.; Fayer, M. D. Dynamics of Water Molecules and Ions in Concentrated Lithium Chloride Solutions Probed with Ultrafast 2D IR Spectroscopy. *J. Phys. Chem. B* **2019**, *123*, 7628−7639.
(54) Hoffman, D. J.; Sokolowsky, K. P.; Fayer, M. D. Direct observation of dynamic crossover in fragile molecular glass formers with 2D IR vibrational echo spectroscopy. *J. Chem. Phys.* **2017**, *146*, 124505.
(55) Shin, J. Y.; Wang, Y.-L.; Yamada, S. A.; Hung, S. T.; Fayer, M. D. Imidazole and 1-Methylimidazole Hydrogen Bonding and Non-hydrogen Bonding Liquid Dynamics: Ultrafast IR Experiments. *J. Phys. Chem. B* **2019**, *123*, 2094−2105.

https://dx.doi.org/10.1021/acs.jpca.0c04313
J. Phys. Chem. A 2020, 124, 5979−5992